PAPER • OPEN ACCESS

A wrist-inspired suspended tubercle-type tensegrity joint with variable stiffness capacity

To cite this article: Xiongdun Xie *et al* 2023 *Bioinspir. Biomim.* **18** 016010

View the article online for updates and enhancements.

You may also like

Bioinspiration & Biomimetics

PAPER

A wrist-inspired suspended tubercle-type tensegrity joint with variable stiffness capacity

Xiongdun Xie[*] , Dezhu Xiong and James Zhiqing Wen

Ji Hua Laboratory, Engineering Research Center for Intelligent Robotics, Foshan, People's Republic of China
* Author to whom any correspondence should be addressed.

E-mail: xiexiongdun@jihualab.com

Abstract

In complex and unpredictable environments or in situations of human–robot interaction, a soft and flexible robot performs more safely and is more impact resistant compared to a traditional rigid robot. To enable robots to have bionic features (flexibility, compliance and variable stiffness) similar to human joints, structures involving suspended tubercle tensegrity are researched. The suspended tubercle gives the joint compliance and flexibility by isolating two moving parts. The variable stiffness capacity is achieved by changing the internal stress of tensegrity through the simultaneous contraction or relaxation of the driving tendons. A wrist-inspired tensegrity-based bionic joint is proposed as a case study. It has variable stiffness and two rotations with a total of three degrees of freedom. Through theoretical derivation and simulation calculation in the NASA Tensegrity RobotToolkit (NTRT) simulator, the range of motion, stiffness adjustable capacity, and their interaction are studied. A prototype is built and tested under a motion capture system. The experimental result agrees well with the theoretical simulation. Our experiments show that the suspended tubercle-type tensegrity is flexible, the stiffness is adjustable and easy to control, and it has great potential for bionic joints.

1. Introduction

In a traditional robot arm, motors and reducers are at or near the joints, so the stiffness and motion accuracy of the joint are high. However, rigid robots are not suitable for unstructured tasks and human–robot interaction because their high inertia may cause serious collision damage to themselves, the human body, and the environment. In other words, rigid robots perform badly when it comes to flexibility and impact resistance. Soft robots are flexible and versatile, but their load capacity is usually limited due to their lack of rigidity [1]. A tendon-driven robot keeps the motor away from the moving arm, thus reducing the inertia of motion and achieving a certain rigid-flexible balance [2]. A variety of tendon-driven robots and joints have been proposed and verified to have low weight, variable stiffness and a certain impact resistance [3–5]. However, tendon transmission alone cannot achieve compliance and impact resistance in all directions because the linkages are still rigid, and the flexibility only exists in the limited directions of tendons transmission.

Tensegrity has essential advantages in keeping the rigid-flexible balance, compliance and impact resistance. The tensegrity-based robot has attracted attention in unstructured tasks and human–robot interaction. A tensegrity structure consists of compression elements (usually rigid rods and frames) and tension elements (usually cables with internal tension) [6, 7]. It can mimic the musculoskeletal system of vertebrates composed of bones, muscles and tendons [8]. The tensegrity structure can be driven by controlling the lengths of some tension units [7], similar to the contraction and relaxation of muscles.

In a mechanical structure consisting of soft and rigid elements, force distribution in the whole structure exists through multiple paths [7]. As a result, a tensegrity structure can withstand force and impact from different directions, and return to the equilibrium position, which can be summarized as structural compliance. Additionally, the rigidity of a tensegrity

can be easily adjusted by changing the tension within the network [9]. Tensegrity structures have been used in bionic shoulders [10], elbows [11], knees [12] and wrists [13, 14].

Ideally, robots should possess the ability to change between stiffness states depending on their surrounding environment and task [15]. Hence, a variable stiffness structure and its control method is highly required in a bionic mechanism. Davide Zappetti *et al* use an active mechanism to add or remove a ball-joint constrain among the vertebrae to achieve a variable-stiffness tensegrity spine [15]. They also use phase changing material to build variable-stiffness cables in tensegrity, demonstrating the ability to act as a beam with tunable load-bearing capability and underactuated joints [16]. Air pressure can also control the stiffness of robot links made of special airtight chambers [17].

Inspired by the above studies, we aim to find a kind of biomimetic structure on the basis of tensegrity that satisfies the following three characteristics: precise control of joint angle; flexibility; stepless adjustment of stiffness. Suspended tubercle type tensegrity meets the above requirements well. Firstly, the suspended tubercle gives the joint compliance and flexibility by isolating two moving parts. Secondly, the relative position of the moving parts is determined by the length of the active tendons evenly set around, so the joint angle is precisely controllable. Finally, by adjusting the compression to the tubercle using active tendons, the inner tension of the whole structure changes continuously.

In order to clarify the bionic design method and its effect based on suspended tubercle tensegrity, a wrist-inspired joint is proposed and the whole process of design, calculation, simulation and experiment is presented in this paper.

The joint has approximately the same performance in all bending directions, which is beneficial for robot control. Through the simulation, we also found that the joint conforms to the characteristic of 'quaternion joint' proposed by Li *et al* [3]. The wrist has two pairs of antagonistic muscles controlled by two motors to achieve universal motion of the joint. At the same time, a third motor is set to synchronously tighten or relax all four muscles to adjust the stiffness of the joint.

The paper is organized as follows. Firstly, the background of the robot joint, tensegrity structure and stiffness adjustable structure are discussed in the introduction. Secondly, the bionic mechanical design of the proposed flexible wrist is analyzed in detail; thirdly, in the section about the mechanism model, the static equilibrium of the mechanism is derived. Fourthly, the NASA Tensegrity RobotToolkit (NTRT) simulator is used to simulate the range of motion (ROM), anisotropic compliance, and variable stiffness characteristics of the flexible wrist. Then, a

prototype is built and tested under a motion capture system and the data is compared with the simulation. The final section summarizes this paper's contribution and the focus of future work.

2. Bionic inspiration

A human wrist assumes important functions of the arm's flexibility. It is located between the forearm and the hand, playing an important role in buffering and orientation. At the same time, due to the wrist's strong variable stiffness capacity, we can wave hands and touch things gently, we can punch and push heavy objects as well.

A human wrist is composed of eight bones connected to each other by ligaments that stabilize the wrist bones when in motion [18]. On the left of figure 1, it can be seen that the eight carpal bones form a mosaic structure. It connects to five metacarpals on one end and to the radius and ulna on the other. Omitting the fingers' movement, the motion of the wrist is mainly the relative motion between the three parts colored green, blue and brown.

The wrist motion is driven by four main muscles: flexor carpi radialis, flexor carpi ulnaris, extensor carpi radialis longus and extensor carpi ulnaris. The palmaris longus is missing in about 15% of modern humans, but it does not affect the wrist's movement [19]. Two pairs of antagonistic muscles dominate a wrist's motion: the flexors and extensors of the radial side and the flexors and extensors of the ulnar side.

A human wrist's ROM in two directions are asymmetric, as listed in table 1 [20], but in order to simplify the model, the two pairs of antagonistic driving tendons of a bionic wrist can be set symmetrically, which has the benefit of freedom decoupling.

Based on the anatomy and motion mode of the wrist, we simplify the wrist as a universal joint in which the two freedoms are controlled by two pairs of active antagonistic muscles. On the right of figure 1, after simplification, the eight carpal bones are put together into one acting as a suspended tubercle between the palm and the forearm. The suspended tubercle connects both ends with elastic material.

The drive method of the bionic wrist is shown in figure 2. The function of the four main muscles are achieved by two groups of antagonistic tendons. They are arranged perpendicular to each other: each tendon passes through the forearm, and is fixed at the corresponding corner of the palm. The distances between the four corners are controlled by the two groups of tendons, and the universal joint is obtained.

The dynamics of the system consisting of forearm, suspended tubercle, palm, four active tendons and serial passive tendons is achieved by a suspended tubercle tensegrity structure. In the next section, the tensegrity is introduced including its self-stress and motions.
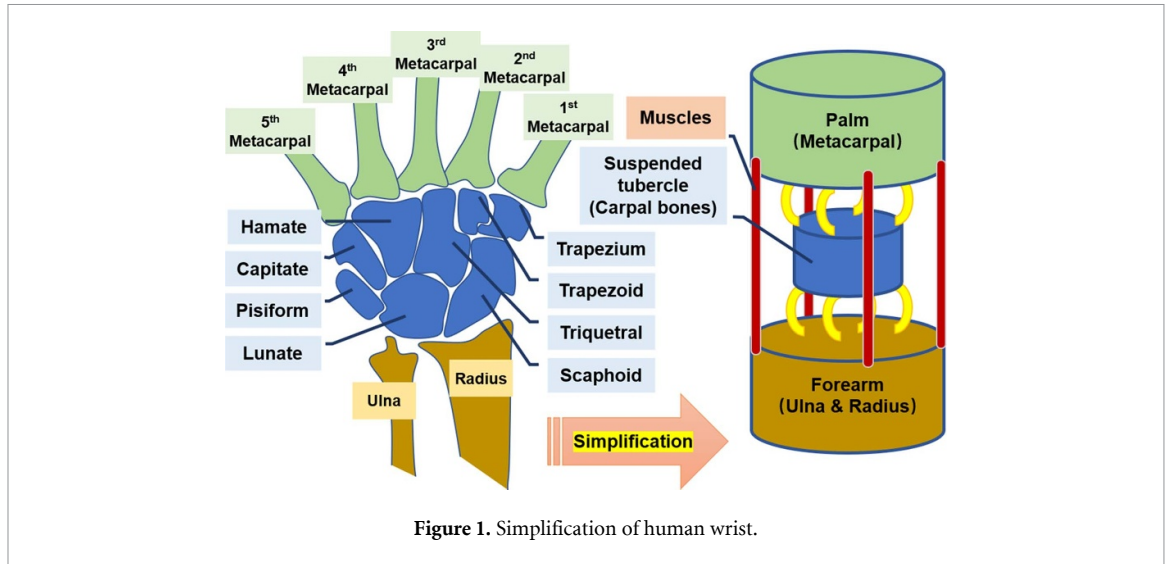
Figure 1. Simplification of human wrist.

Table 1. Human wrist's ROM.

Motion	ROM
Palmar flexion	$0°–70°$
Dorsiflexion	$0°–60°$
Ulnar abduction	$0°–30°$
Radial abduction	$0°–20°$

Figure 3. Flexible wrist mechanism model.

figure 3(a). Figure 3(b) presents the structure of the carpal bone and connection node locations $N_9 \sim N_{16}$. The palm and the forearm are directly connected by the active driving tendons $q_1 \sim q_4$. q_1 and q_3 are wrapped to a wheel antagonistically, while q_2 and q_4 have the same driving model. Passive elastic elements are also used to connect the palm, forearm and carpal bone. Figure 3(c) shows the arrangements of those passive elastic elements with labels $q_5 \sim q_{12}$ that bind carpal to the bone and forearm symmetrically. Elements $q_{13} \sim q_{20}$ connect the palm and carpal bone.

There are two types of nodes in the system: $N_1 \sim N_8$ and $N_9 \sim N_{16}$. We focus on the former because they are the outer nodes and are connected to the driving tendons. Taking N_5 as an example, it is located in the palm rigid body. All the nodes of this rigid body are on the $N_5 \sim N_8$ plane, so only when the resultant force of q_1, q_{13} and q_{14} is on the plane, can the node N_5 maintain balance. As shown in figure 3(a), in the neutral position, the forearm and the palm are parallel, and the wrist does not flexor or deviate. The tensile
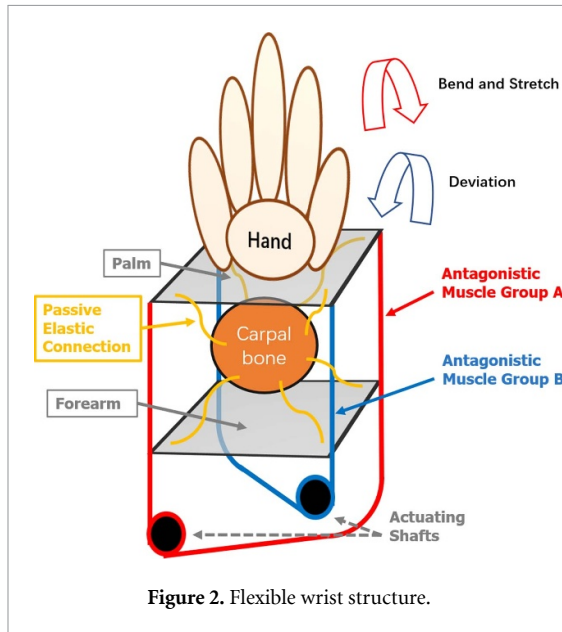

Figure 2. Flexible wrist structure.

3. Wrist model

3.1. Tensegrity structure

The proposed tensegrity-based wrist with variable stiffness will be introduced in detail in this section. As shown in figure 3(d), there are three rigid parts: forearm, palm and carpal bone. The forearm and the palm have the same structure but they are located colinear and orientated to each other. Symmetric nodes $N_1 \sim N_4$ and $N_5 \sim N_8$ are attached to the forearm and palm, respectively, as shown in
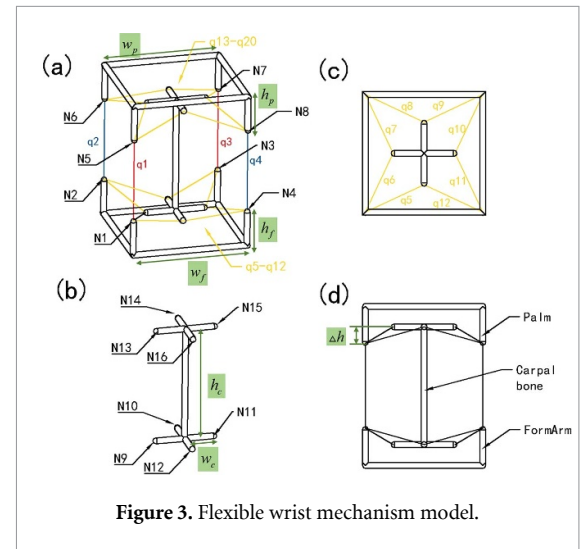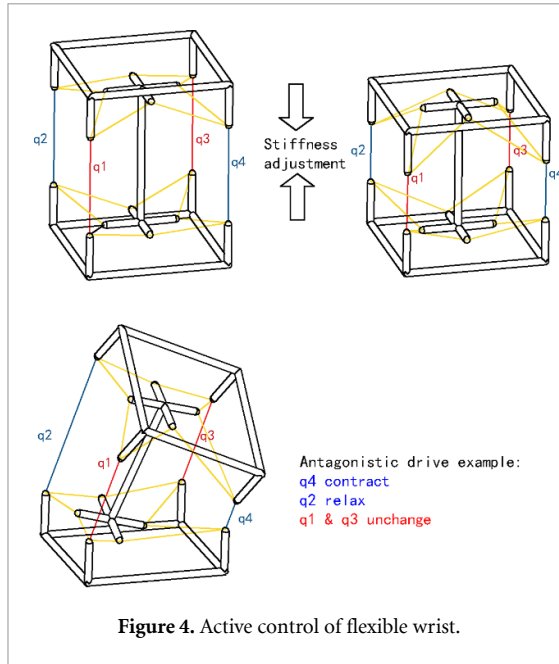
Figure 4. Active control of flexible wrist.

force F_{q1} is straight down, while the component of F_{q13} and F_{q14} in the vertical direction is $K_s \triangle h$, where K_s is the stiffness of the passive elastic spring (yellow element in figures 3 and 4), $\triangle h$ is the height difference between N_5 and N_{13} (or N_{16}). As long as $\triangle h > 0$ for each of $N_1 \sim N_8$, The system meets the requirements for self-equilibrium.

The flexible wrist forms a tensegrity self-balancing network. The four vertical active muscles make the wrist have a tendency to contract . With the carpal bone 'squeezed', the passive elements resist the contraction and draw a static balance. The magnitude of self-stress is determined by $K_s \triangle h$, so there are two ways to change the stiffness of the network: one is selecting springs of different K_s; the other is changing the length of $q_1 \sim q_4$, thus changing $\triangle h$. The latter is the key that the stiffness of the system can be adjusted steplessly through four active cables.

Figure 4 shows the drive modes of the wrist. When four muscles contract or relax synchronously, the internal tension of all the cables increases or decreases, and the stiffness is changed. When the two antagonistic tendon groups are driven differently, the wrist bends from the neutral state and performs flexion or deviation. As shown in figure 4, the 16 passive tendons have unbalanced loads at this moment. The ligaments on the compressed side are elongated, and those on the relaxation side are shortened, reaching a new balance of lateral force.

Both active muscles and passive ligaments must move within the ROM and tension, to ensure that they do not snap, loosen, or collide between rigid bodies, to prevent joint failure. The above joint's failures correspond to muscle rupture, ligament laxity, and impact bone disease in human joints.

3.2. Static equilibrium of tensegrity

For the conventional mechanism, the configuration can be calculated accurately by kinematics when the position of the actuator is given. However, for tensegrity mechanisms, the degrees of freedom associated with the tension components are unconstrained and the mechanism can deform even if the actuator is locked [21]. Therefore, the configuration of the mechanism can only be calculated by using static equilibrium. Without external forces, a tensegrity mechanism is a conservative system, and its static equilibrium condition can be obtained by minimizing the total potential energy of the system with respect to independent generalized coordinates [21]. In terms of our proposed flexible wrist structure, the states of the carpal bone and the palm must be taken into consideration in static equilibrium. The independent generalized coordinates of the carpal bone can be set as $q_i, i = 5 \sim 10$ (random six within $i = 5 \sim 12$) and palm as $q_i, i = 1 \sim 4 \cup (13, 14$ or $15, 16$ or $17, 18$ or $19, 20)$, The static equilibrium equation of the whole system is derived as equation (1):

$$-\frac{\partial V}{\partial q_i} = 0, i = 1 \sim 10, 13, 14 \qquad (1)$$

where V is the total potential energy, consisting of elastic potential energy V_s and gravitational potential energy V_ω given in equation (2), and they are derived as equations (3)–(7)

$$V = V_s + V_\omega \qquad (2)$$

$$V_s = \sum_{i=1}^{20} \frac{1}{2} k_i \left(q_i - q_{fli} \right)^2 \qquad (3)$$

$$V_\omega = m_p g \cdot h_p + m_c g \cdot h_c \qquad (4)$$

$$q_j = L_j \left(q_1, q_2, \ldots, q_{10}, q_{13}, q_{14} \right), j = 11, 12, 15 \sim 20 \qquad (5)$$

$$h_c = H_c \left(q_1, q_2, \ldots, q_{10} \right) \qquad (6)$$

$$h_p = H_p \left(q_1, q_2, \ldots, q_{10}, q_{13}, q_{14} \right) \qquad (7)$$

where k_i, q_{fli} and q_i are the stiffness, free length and equilibrium length of each tendon respectively, L_j is the relation between $q_j, j = 11, 12, 15 \sim 20$ and independent generalized coordinates; m_p and m_c the mass of palm and carpal bone respectively; h_p and h_c are the heights between the barycenter of the palm and carpal bone to the gravity potential energy datum respectively (the gravity potential energy datum is selected according to the actual situation). When this surface passes through the barycenter of the forearm, the forearm has no gravity potential energy. H_p and H_c

are the geometric relations between h_p and h_c to q_i respectively.

Substituting equations (2)–(7) into equations (1) and (8) gives the static equilibrium equation of the tensegrity system:

$$
k_i \left(q_i - q_{\text{fli}} \right) + \left(\sum_{j=11,12,15\sim20} k_j \left(L_j - q_{\text{flj}} \right) \frac{\partial L_j}{q_i} \right) \\
+ m_p g \frac{\partial H_c}{\partial q_i} + m_c g \frac{\partial H_p}{\partial q_i} = 0, i = 1 \sim 10, 13, 14
$$

(8)

4. Simulation and analysis

4.1. Model setting
NTRTsim is used to simulate the behavior of a system. NTRTsim uses a Cartesian mapping system to describe the geometry of tensegrity structures and Euler–Lagrange formulas to describe dynamics to predict the elastic forces inside elastic cables [22]. NTRTsim has been used in the simulation of various tensegrity joints by other researchers [10–12].

According to the mechanism description section 3, the flexible wrist is modeled in NTRTsim for the subsequent simulation calculation. Table 2 presents the important parameters. The dimension parameters are plotted in figures 3(a) and (b).

4.2. ROM
The ROM is determined by the movement scale of the driving cable. The length of the driving cable can be calculated by equation (9):

$$
q_i = q_n + A_q \cdot \sin\left(f \cdot t + \frac{2\pi \cdot i}{4} \right), i = 1 \sim 4, \quad (9)
$$

$$
\begin{bmatrix} Q_w \\ Q_x \\ Q_y \\ Q_z \end{bmatrix} = \begin{bmatrix}
\cos\left(\frac{\varphi}{2}\right)\cos\left(\frac{\theta}{2}\right)\cos\left(\frac{\psi}{2}\right) + \sin\left(\frac{\varphi}{2}\right)\sin\left(\frac{\theta}{2}\right)\sin\left(\frac{\psi}{2}\right) \\
\sin\left(\frac{\varphi}{2}\right)\cos\left(\frac{\theta}{2}\right)\cos\left(\frac{\psi}{2}\right) - \cos\left(\frac{\varphi}{2}\right)\sin\left(\frac{\theta}{2}\right)\sin\left(\frac{\psi}{2}\right) \\
\cos\left(\frac{\varphi}{2}\right)\sin\left(\frac{\theta}{2}\right)\cos\left(\frac{\psi}{2}\right) + \sin\left(\frac{\varphi}{2}\right)\cos\left(\frac{\theta}{2}\right)\sin\left(\frac{\psi}{2}\right) \\
\cos\left(\frac{\varphi}{2}\right)\cos\left(\frac{\theta}{2}\right)\sin\left(\frac{\psi}{2}\right) - \sin\left(\frac{\varphi}{2}\right)\sin\left(\frac{\theta}{2}\right)\cos\left(\frac{\psi}{2}\right)
\end{bmatrix},
$$

(10)

$$
Q_x = A_Q \cdot \sin\left(f \cdot t + \frac{\pi}{2} \right), \quad (11)
$$

$$
Q_z = A_Q \cdot \sin\left(f \cdot t \right), \quad (12)
$$

where:

q_n is the neutral length of the driving tendons;

A_q is the amplitude of the length;

f is the frequency of the motion;

Q_w, Q_x, Q_y, Q_z are the four components of the joint's quaternion, representing the joint deflection angle and the rotation angle around the *x, y* and *z* axes.

q_n and A_q determine the ROM, while *f* determines the period of motion. q_n and A_q are set to keep the joint from collision or losing tension, but reaching the maximum ROM. The driver parameter settings are shown in table 1.

The stimulation process is demonstrated in figure 5. During the motion, the *y*-coordinate value of the centroid of the palm basically remained unchanged, with a standard deviation of 0.025 mm. The relation between *x* and *y* is shown in figure 6. The trajectory is close to a perfect circle.

The Euler angle output of the simulation is converted into quaternion form using equation (10). Under the drive control of equation (9), the joint's quaternion over time is shown in figure 7.

Q_w is nearly constant, indicating that the deflection angle of the joint is also nearly constant. The deflection angle is 32.54° and the standard deviation is 0.34°, indicating that there is a strong symmetry between the drive space and the joint motion space. Figures 5(a) and (b) show two configurations under boundary conditions: single antagonistic limit (figure 5(left)) and double antagonistic limit (figure 5(right)). The former refers to a pair of antagonistic muscles in the shortest contraction (q1) and longest extension state (q3) respectively, while the other group of antagonistic muscles are in a neutral location (q2, q4); the latter refers to the two pairs of antagonistic muscles that both reach the state where one muscle is in the shortest contraction (q1, q2) and the other in the longest extension state (q3, q4). The joint angles of the single antagonistic limit and the double antagonistic limit are 31.25° and 33.65° respectively, which are not equal, indicating that the joint did not achieve the ideal symmetry of drive and deflection.

Q_y is basically zero, indicating that rotation about the *y*-axis is not included in the motion mode of the joint.

Q_x and Q_z over time are shown in equations (10) and (11). In the model shown in figure 7, and the corresponding antagonistic muscle on the *x*-axis are q1 and q3, and those on the *z*-axis are q2 and q4, so

Table 2. Parameter setting.

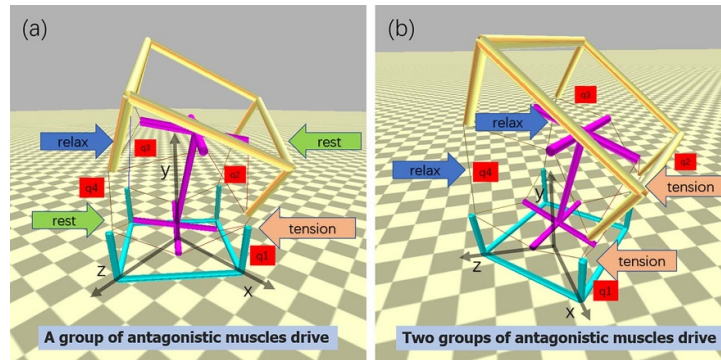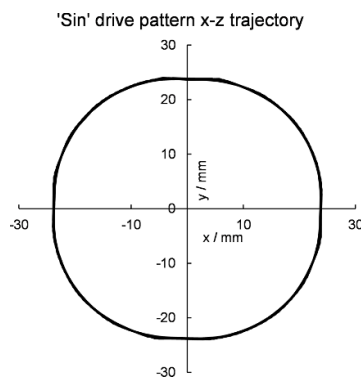| Physical parameter	
m_p	0.163 kg
m_c	0.244 kg
s	800 N m^{-1}
C	10Ns m^{-1}
Dimension parameter	
w_f, w_p	0.05 m
h_f, h_p	0.03 m
w_c	0.02 m
h_c	0.06 m
Drive parameters	
q_n	0.03 m
A_q	0.03 m
f	2 s^{-1}

Figure 5. Joint's ROM simulation.

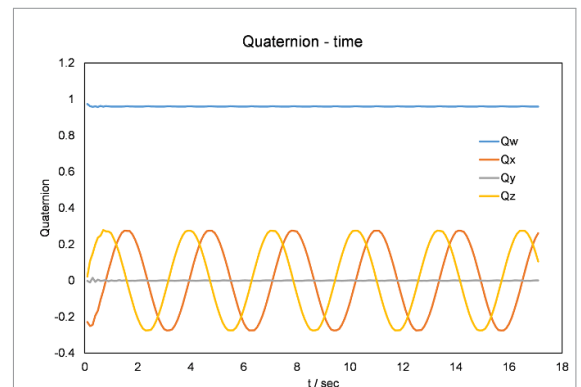**Figure 6.** Circular trajectory of the palm.

Figure 7. Quaternions over time.

the tendon space described in equation (8) and the joint quaternion space described in equations (10) and (11) are decoupling correspondingly. The driving method of this joint is consistent with that of the AMBIDEX quaternion joint [3]. A similar effect is achieved by using a different mandrel mechanism.

4.3. Joint stiffness adjustment
Our flexible wrist is capable of stiffness adjustment. Specifically, the neutral lengths of $q_i, i = 1 \sim 4$ are adjusted synchronously and simultaneously, to achieve the relaxation and tightening of the overall structure, resulting in different stiffnesses.

The stiffness simulation model is set as shown in figure 8: a loading point is set in the center of the palm. Three external force points are set: along the y-axis, x-axis and bisecting angle between the x- and z-axis. By exporting the loading forces and the displacements along the forces through simulation,
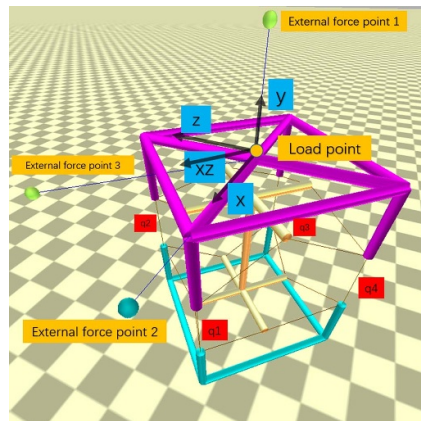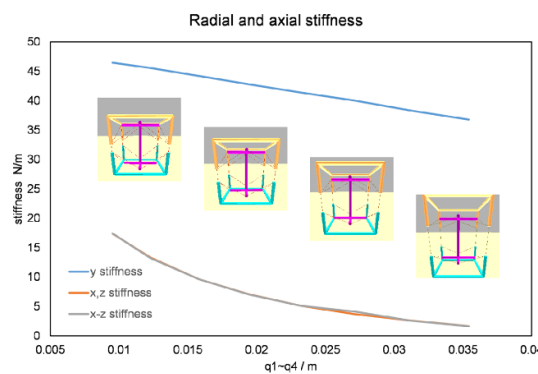
Figure 8. Stiffness simulation setting.

Figure 9. Length–stiffness curve of driving tendon.

Figure 10. Radial stiffness—ROM.

the stiffness in different directions can be calculated according to its definition.

The axial and radial stiffness of joints were obtained by adjusting $q_i, i = 1 \sim 4$ to different lengths, and the results are shown in figure 9. When $q_i, i = 1 \sim 4$ are shortened within $[0.01, 0.035]$ m, the axial stiffness linearly increases within $[36.77, 46.47]$ N m^{-1}. It can be seen from figure 9 that the radial stiffness of the joint has strong symmetry, because the stiffness along the x-axis and along the bisect angle between the x- and z-axis are basically the same, with logarithmic growth within $[1.63, 17.44]$ N m^{-1}. The axial stiffness is mainly dominated by four vertical driving tendons, so the axial stiffness increases linearly with compression of the joint. The radial stiffness is mainly dominated by passive wrist ligaments, so as the angle of ligaments changes with the compression of joints, the radial stiffness changes nonlinearly.

It should be noted that the joint stiffness is negatively correlated with the ROM of the joint. Since the radial stiffness of the joint is small, only the relationship between the radial stiffness and the ROM is considered. As shown in figure 10, the ROM of the joint $[5°, 30°]$ corresponds to the range of the radial stiffness $[13 \text{ N m}^{-1}, 2.5 \text{ N m}^{-1}]$. Therefore, in practical applications, the requirements of ROM should
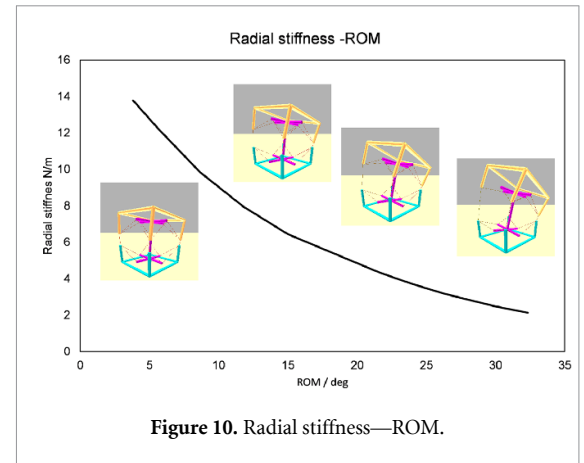
be considered when controlling the stiffness of the joint, and certain trade-offs should be made.

5. Prototype design and experiment

In order to verify the decoupled motion, variable stiffness capacity and the relationship between the motion range and the stiffness of the proposed flexible wrist, a prototype was designed, manufactured, and tested in an experimental rig. The wrist motion and variable stiffness experiments were carried out. The motion data was obtained by an optic motion capture system, and compared with the simulation data under the same setting.
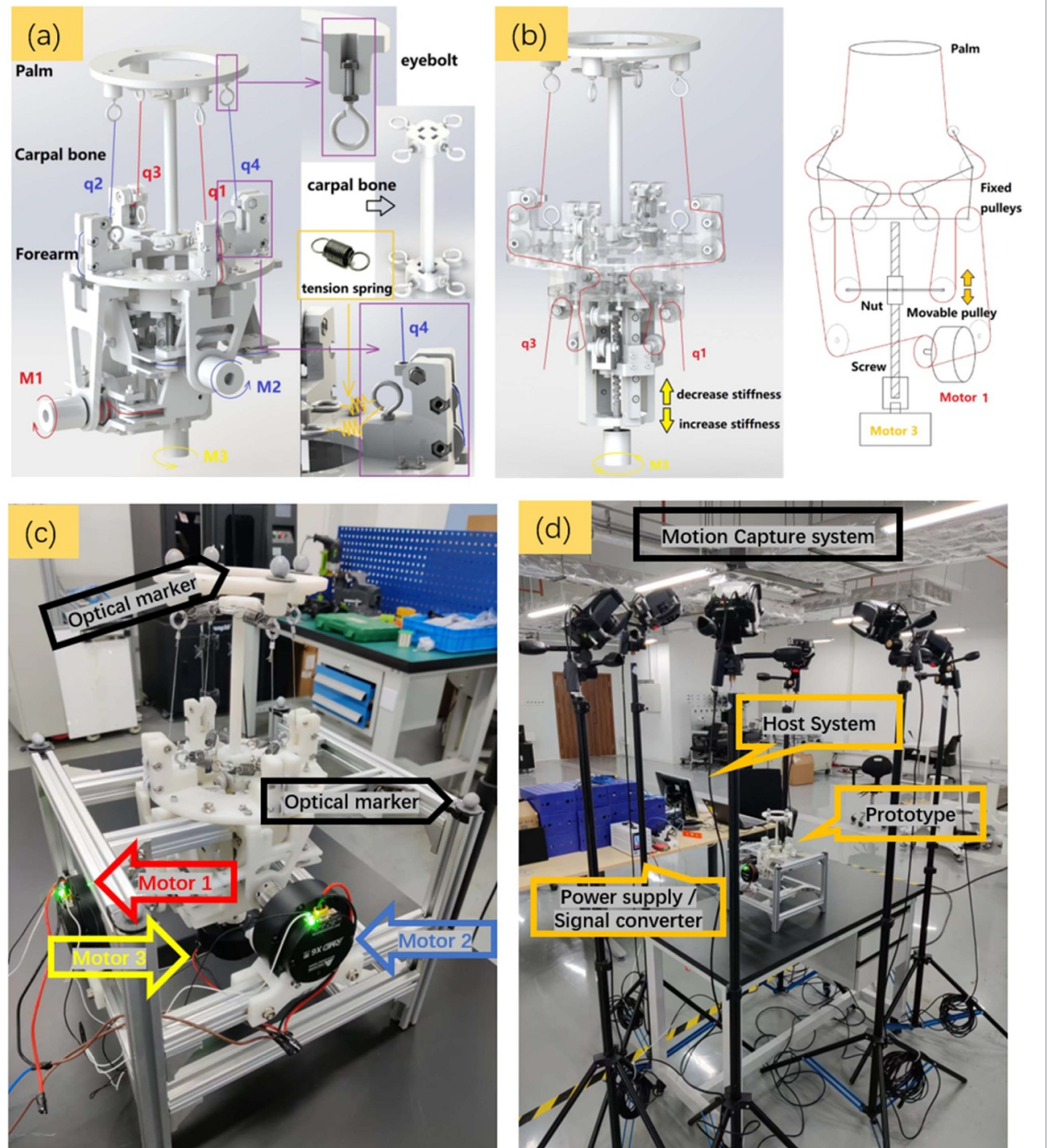
5.1. Prototype and test rig set up

Figure 11(a) presents the mechanism diagram of the prototype. The palm part is annular with four sling bolts for tension spring connection, corresponding to $N_5 \sim N_8$. The structure of the carpal bone part is similar to the that shown in figure 3(b), and the connecting function of the nodes is also realized by the sling bolt, corresponding to $N_9 \sim N_{16}$

The forearm assumes the function of the tendon drive chain, so the structure is relatively complex. Four sling bolts corresponding to $N_1 \sim N_4$ are set. Motion interference will occur if both spring connection and active tendon-rope guidance are achieved in the same sling ring, so, as shown in the detailed view in the bottom right of figure 11(a), $N_1 \sim N_4$ are divided into two structures: the sling ring realizes the connection of the passive ligament, and the active tendons go through the guide holes. The two connection points are set close enough to minimize the error with the simulation model. According to the measurement, the stiffness of the tension spring selected as the passive ligament is 800 N m^{-1}, which is the same in the simulation model as shown in table 2. The dimensions of the prototype also follow table 2. Besides the manufacture error, the self-stress of the prototype is close to the simulation model.

According to the design idea in figure 2 and the control logic shown in figure 4, q_1 and q_3, q_2 and q_4 are two pairs of antagonistic tendon ropes. As shown

Figure 11. Prototype and test rig. (a) Structure of wrist prototype, (b) degree of freedom for stiffness adjust, (c) prototype marked with motors and optical marker, (d) experimental rig.

in figure 11, they are twined on two capstans M_1 and M_2 respectively. How M_3 controls the joint stiffness is shown in figure 11(b): M_3 drives the screw, and four pulleys fixed on the nut can move simultaneously. The path of q_1 and q_3 are shown, while q_2 and q_4 are the same on the vertical plane. The schematic diagram in the right of figure 11(b) shows: when the movable pulley moves downward, both tendons are tensioned so the palm is pulled down tight and its stiffness increases. On the contrary, when the movable pulley moves upward, the tendons are relaxed, resulting in the decrease in stiffness. This way of adjusting the stiffness by changing the path of the tendons does not affect the antagonistic drive of the wrist. Motor 1 is one of the antagonistic drive motors, as shown in the schematic diagram, its function is not affected by

motor 3. In fact, they can work at the same time, resulting in the wrist deflecting and tightening or relaxing simultaneously.

Figures 11(c) and (d) show the prototype and the experimental rig correspondingly. Our prototype is fixed on an aluminum base, and the main body is 3D printed pieces. Three motors are connected to the prototype through coupling. The whole experimental setup consists of the prototype, motion capture system, power supply, Controller Area Network to Universal Serial Bus signal converter (CAN—USB) and host machine. The motion commands are sent to the motor through the signal converter from the upper computer. The motion capture system has six cameras in different poses, optical markers are attached on interested parts as in figure 11(c). The
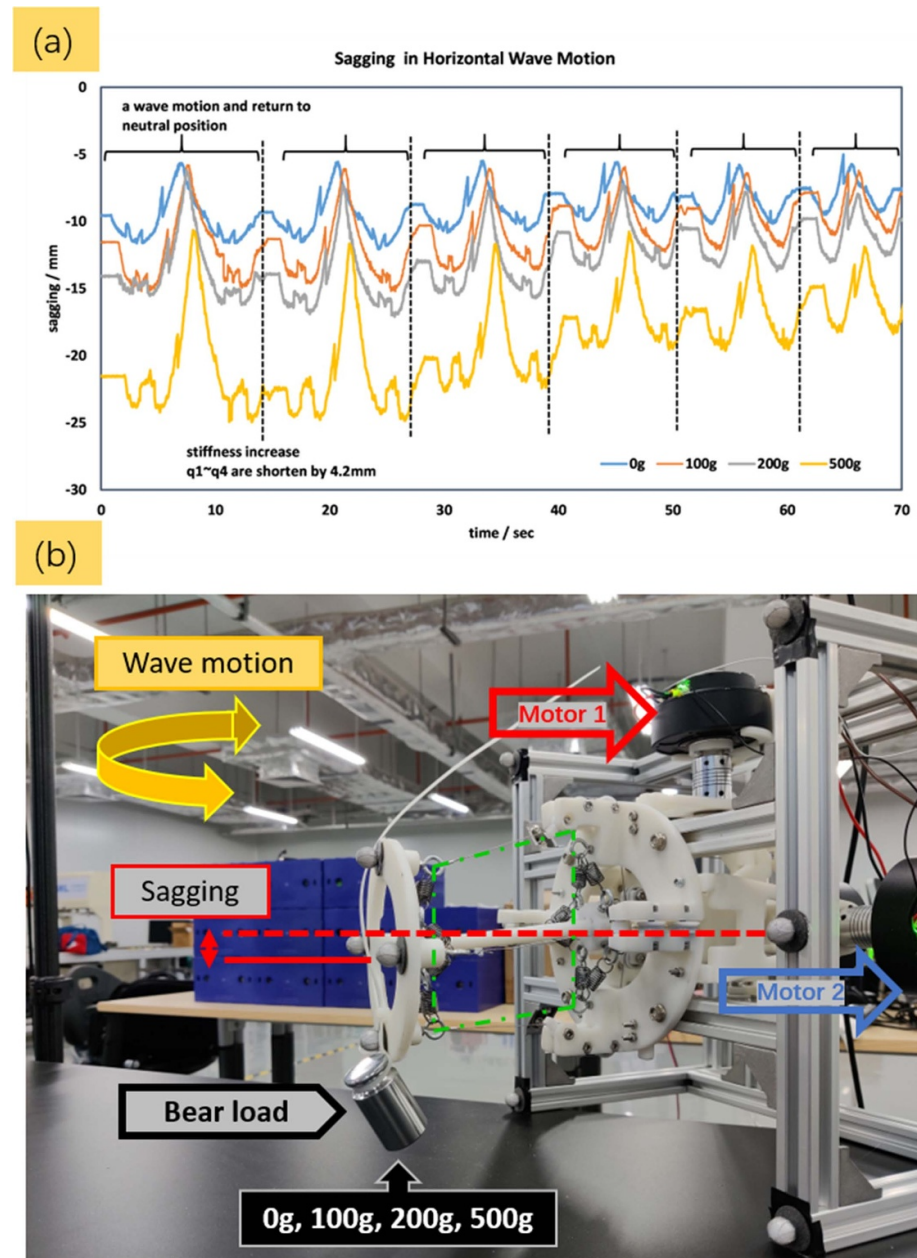
Figure 12. Sagging measurement in horizontal wave motion: (a) sagging distance during horizontal wave motion (joint's stiffness increased periodically; different bear load). (b) Prototype set horizontally.

motion capture system is able to record movement at 60 frames per second and with a 0.01 mm tracking accuracy.

In order to test the deflection of the flexible wrist when the lateral force is applied corresponding to the *x* or *z* force in figure 8, we also position the prototype sideways so that the palm can be horizontally loaded. As shown in figure 12(b), different weights can be hung on the palm, and the motion experiment was carried out under this condition. Before the prototype is set horizontally, the wrist is adjusted to a neutral position so that the mark points on the palm align to those on the base, so the sagging distance can be calculated easily. As shown in figure 12(b), the sagging distance is defined as the drift from the center of the base to the palm center.

5.2. Experiments and data analysis

We conducted wrist movement experiments both in the NTRT simulator and in the real world and compared the results. In the NTRT simulator, the length of the four active tendons can be directly controlled, while on the prototype, their movements are controlled by three motors. After conversions of unit, transmission coefficient and coordinates, the prototype and simulation data are plotted together: the dashed line is the simulation data, and the solid line with corresponding colors is the prototype motion experiment data. The data are all about the palm part because it is the output side we care about.

(a) Stiffness increase motion: wrist maintains a neutral position while periodically shortening
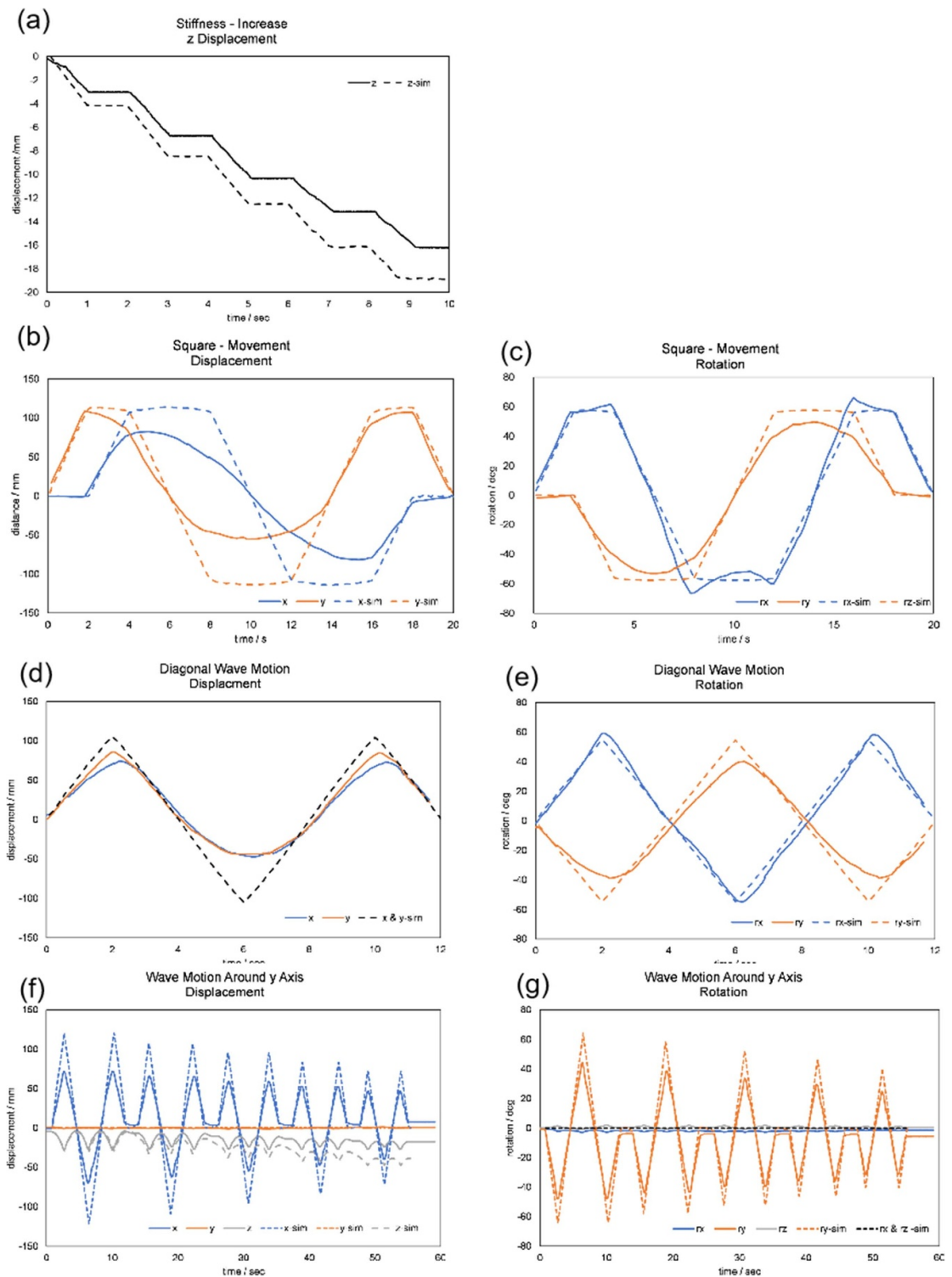
Figure 13. Motion capture data (solid) compared with simulation result (dash): (a) stiffness increase motion *z* displacement, (b) square-shape motion displacement, (c) square-shape motion rotation. (d) Diagonal wave motion displacement, (e) diagonal wave motion rotation. (f) Wave motions with stiffness increase displacement, (g) wave motions with stiffness increase rotation.

the length of the four driving tendons, as described in figure 4, the stiffness adjustment mode. The curve of the palm part displacement along the *z*-axis over time is shown in figure 13(a).

(b) Square-shape motion: starting from the neutral position, the palm part first reaches the limit angle around the *x*-axis then reaches the limit angle around the *y*-axis, and then circulates, successively reaching the four symmetric limit
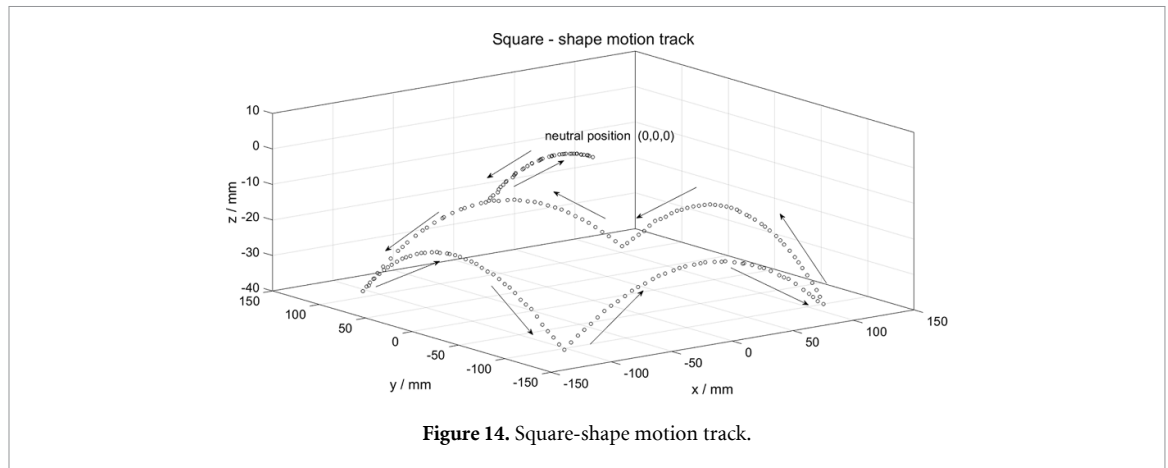
Figure 14. Square-shape motion track.

positions and returning to the neutral position. Figure 14 shows the track of the square-shape motion.

Figures 13(b) and (c) show the displacement along the x- and y-axes and the rotation angles around the x- and y-axes over time in square-shape motion.

(c) Diagonal wave motion: the palm part moves synchronously around the x- and y-axes to reach the limit on both sides, and then returns to the neutral position. Figures 13(d) and (e) show the displacements and rotation data in diagonal wave motion

(d) Multiple one-direction wave motions with stiffness increase: the palm part only rotates about the y-axis, with the stiffness of the wrist increasing, the amplitude of the wave decreasing. The remaining length of the active tendons should be maintained at 3 mm to prevent collision between the palm and the forearm. Figures 13(f) and (g) show the displacements and rotation data in stiffness increasing multiple one-direction wave motions.

(e) Multiple horizontal one-direction wave motions with stiffness increase under different bear loads: as shown in figure 12(b), different weights are hung on the palm in turn. The yellow arrow indicates the direction of wave motion which is the same as '4. Multiple one-direction wave motions with stiffness increase'. Figure 12(a) shows the sagging (z-axis displacements) during the motions. In the time range in every parenthesis, the palm completes one wave and returns to the neutral position. At every timepoint marked by dashed lines, motor 3 worked to shorten $q_1 \sim q_4$ by 4.2 mm.

From figure 13, it can be concluded that:

(a) The prototype is in good agreement with simulation: the trend of the curves of displacement and rotation angle are consistent.

(b) The amplitude of the prototype is smaller than that of the simulation under various motions, that is, the value of the solid line is smaller than that of the dashed line on the whole.

(c) In the simulation, the joint is completely decoupled in the two rotational motion directions, while there is a certain degree of coupling in the prototype: In figure 13, the dotted curve has some horizontal platforms, which means that the motion in one direction will not affect the rest in the other direction, proving that the two vertical rotational motions are decoupled. But the platform of the solid line is tilted or with arcs, which means in the prototype, the two rotational motions are not completely decoupled.

From figure 12(a), the sagging problem is summarized:

(a) Due to the flexible connection in the wrist, the sagging phenomenon exists. Self-weight makes the palm flap down of 9.5 mm, and the sagging distance increases proportionally with the bear load.

(b) During the waving motion, the palm fluctuates. When palm deflects to one side, the sagging distance is the least for the palm is closer to the base thus with a higher stiffness.

(c) The sagging distance decreases with the increase in joint stiffness which conforms to the simulation.

The corresponding analysis of the above data and reasons for the existence of errors can be made as follows:

(a) The feasibility of the proposed bionic wrist based on the tensegrity structure with variable stiffness is verified: the joint has variable stiffness and two rotations with a total of three degrees of freedom.

(b) The small motion amplitude of the prototype compared to the simulation is caused by low stiffness and hysteresis in the tendon-driven

mechanism: the main body of the prototype is plastic with low stiffness, so with the increase in tendon tension, the path of the tendon will be shortened due to the deformation of the main body. As a result, the same capstan rotation angle corresponds to less tendon movement. As shown in figure 13(a), when the wrist stiffness increases, the amplitude of each step of downward motion is lower than that of the simulation, and the gap increases with the increase in contraction times. Also, the amplitudes of the one-direction wave of the prototype shown in figures 13(f) and (g) is lower than that of the simulation; on the other hand, the wrist is driven by two groups of antagonistic tendons without tension control for each tendon, so the imbalance in tension will cause retardation of motion, particularly near the limit position.

(c) The prototype did not realize the complete decoupling of the two rotation directions, and there were many reasons, such as insufficient stiffness of the prototype, deviation of design from the ideal model and errors from machining and assembly. First, when the movement was near the limit position, the structural parts were deformed to a certain extent because of the tension. Therefore, the acquired motion data itself had errors. Second, as shown in figure 7, in the ideal model, tensegrity rods and cables are all connected on ideal points. While in the prototype, the connection of nodes is realized by the connection between the rings. The rings of the spring and tendon rope will slide freely during joint movement, resulting in the change of tensegrity configuration, and the resulting asymmetric factors affect the characteristics of the joint. Third, the parts have parameters and size deviation. For example, unequal spring stiffness leads to tensegrity asymmetry, and the actual nodes cannot be completely symmetric and perpendicular to each other during assembly.

(d) As shown in the simulation result plotted in figure 9: the wrist tensegrity has a relatively lower stiffness on the horizontal plane, so a sagging problem exists on the nonvertical plane. The problem can be reduced by increasing joint stiffness but cannot be eliminated. However, the parallelogram structure of the tensegrity maintains the palm's posture. As shown in figure 12(b), the parallelogram mechanism in tensegrity, marked by green dashed lines, keeps the palm parallel to the base. So, the sagging problem of the wrist can be compensated by the adjustment of upper joints (elbow joint).

6. Conclusion

In this paper, the suspended tubercle type tensegrity combined with a tendon-driven mechanism is used to mimic the musculoskeletal system of human joints. The bionic joint satisfies three main requirements: precise control of the joint angle; flexibility; stepless adjustment of stiffness. In order to verify the biomimetic design method, a bionic joint inspired by the human wrist is proposed, bringing the flexibility and dexterity characteristics that traditional rigid joints do not have. The joint's stiffness can be actively controlled. The joint is a 'quaternion joint' which means the two drives correspond to two of the joint's quaternions.

Analytical, numerical, as well as experimental results, show the feasibility of the proposed joint and also the biomimetic design method based on active suspended tubercle type tensegrity.

Tensegrity joints are expected to improve the performance of robots in unstructured tasks. More work will be carried out in the future:

(a) Numerical calculation of suspended tubercle-type tensegrity's static balance: according to the actual working conditions, the tensegrity structure and its parameters are determined by calculation and optimization.

(b) This paper only explored and verified the joint kinematics, and the performance of the variable stiffness function and compliance in the actual scene needs to be verified. Therefore, a more accurate prototype that is close to engineering application needs to be designed and manufactured.

(c) Tensegrity joint control: joint calibration and motion control determine the practical application. In the future, machine vision and some closed-loop control methods integrated with machine learning may be combined to improve the end control accuracy, for example, compensation of the sagging effect.

ORCID iDs

Xiongdun Xie ⓘ https://orcid.org/0000-0003-1081-8239
Dezhu Xiong ⓘ https://orcid.org/0000-0002-8921-1706
James Zhiqing Wen ⓘ https://orcid.org/0000-0003-0144-5733

References

[1] Terryn S, Brancart J, Lefeber D, Van Assche G and Vanderborght B 2017 Self-healing soft pneumatic robots *Sci. Robot.* **2** eaan4268

[2] Lens T and von Stryk O 2012 Investigation of safety in human-robot interaction for a series elastic, tendon-driven robot arm *2012 IEEE/RSJ Int. Conf. on Intelligent Robots and Systems(IROS)* (*Vilamoura-Algarve, Portugal, 7–12 October 2012*) (https://doi.org/10.1109/IROS.2012.6386236)

[3] Kim Y J, Kim J I and Jang W 2018 Quaternion joint: dexterous 3-DOF joint representing quaternion motion for high-speed safe interaction *2018 IEEE/RSJ Int. Conf. on Intelligent Robots and Systems (IROS)* (*Madrid, Spain, 1–5 October 2018*) (IEEE) (https://doi.org/10.1109/IROS.2018.8594301)

[4] Li W *et al* 2020 Modularization of 2- and 3-DoF coupled tendon-driven joints *IEEE Trans. Robot.* **99** 1–13

[5] Shah D, Parmiggiani A and Kim Y J 2020 Constant length tendon routing mechanism through axial joint *2020 IEEE/ASME Int. Conf. on Advanced Intelligent Mechatronics (AIM)* (*Boston, MA, USA, 5 August 2020*) (IEEE) (https://doi.org/10.1109/AIM43001.2020.9158889)

[6] Motro R 2003 *Tensegrity: Structural Systems for the Future* (Sterling, VA: Kogan Page Science) (https://doi.org/10.1016/B978-1-903996-37-9.X5028-8)

[7] Liu Y, Bi Q, Yue X, Wu J, Yang B and Li Y 2022 A review on tensegrity structures-based robots *Mech. Mach. Theory* **168** 104571

[8] Levin S M 2002 The tensegrity-truss as a model for spine mechanics: biotensegrity *J. Mech. Med. Biol.* **2** 375–88

[9] Kimber J, Ji Z, Petridou A, Sipple T, Barhydt K, Boggs J, Dosiek L and Rieffel J 2019 Low-cost wireless modular soft tensegrity robots *Proc. 2nd IEEE Int. Conf. on Soft Robotics* (Seoul: IEEE) pp 88–93

[10] Baltaxe-Admony L B, Robbins A S, Jung E A, Lessard S, Teodorescu M, SunSpiral V and Agogino A 2016 Simulating the human shoulder through active tensegrity structures *Proc. ASME 2016 Int. Design Engineering Technical Conf. and Computers and Information in Engineering Conf. (IDETC/CIE 2016)* (Charlotte, NC: ASME) pp 1–6

[11] Lessard S, Bruce J, Jung E, Teodorescu M, Sunspiral V and Agogino A 2016 A lightweight, multi-axis compliant tensegrity joint *Proc. IEEE Int. Conf. on Robotics and Automation (ICRA)* (Stockholm: IEEE) pp 630–5

[12] Jung E, Ly V, Castro D and Teodorescu M 2018 Knee-inspired tensegrity flexural joint *2018 Ubiquitous Robots (UR)*

[13] Hong G Y and Choi Y 2019 Tensegrity wrist mechanism using three layers of rigid bodies and strings *2019 16th Int. Conf. on Ubiquitous Robots (UR)* (*Jeju, Korea (South), 25 July 2019*) (https://doi.org/10.1109/URAI.2019.8768647)

[14] Sun J, Cao X and Song G 2020 Design method for a bionic wrist based on tensegrity structures *Biosurf. Biotribol.* **6** 31–36

[15] Zappetti D, Arandes R, Ajanic E and Floreano D 2020 Variable-stiffness tensegrity spine *Smart Mater. Struct.* **29** 075013

[16] Zappetti D, Jeong S H, Shintake J and Floreano D 2019 Phase changing materials-based variable-stiffness tensegrity structures *Soft Robot.* **7** 362–9

[17] Agostino Stillihelge A, Wurdemann H A and Althoefer K 2017 A novel concept for safe, stiffness-controllable robot links *Soft Robot.* **4** 16–22

[18] Behnke R S 2006 Kinetic anatomy *The Wrist and Hand* 4th edn (Human Kinetics)

[19] Reimann A F, Da Seler E H, Anson B J and Beaton L E 1944 The palmaris longus muscle and tendon. a study of 1600 extremities *Anat. Rec.* **89** 495–505

[20] Lalani I and Argoff C E 2010 History and physical examination of the pain patient *Raj's Practical Management of Pain* 4th edn, ed H T Benzon, J P Rathmell, C L Wu and D C Turk (Philadelphia, PA: Mosby) ch 10, pp 177–88

[21] Arsenault M and Gosselin C M 2007 Static balancing of tensegrity mechanisms *J. Mech. Des.* **129** 295–300

[22] Bruce J, Caluwaerts K, Iscen A, Sabelhaus A P and SunSpiral V 2014 Design and evolution of a modular tensegrity robot platform *2014 IEEE Int. Conf. on Robotics and Automation (ICRA)* (*Hong Kong, China, 31 May–7 June 2014*) (IEEE) pp 3483–9